Benchmark numerical simulations of rarefied non-reacting gas flows using an open-source DSMC code

Computers and Fluids 120 (2015) 140–157

Benchmark numerical simulations of rarefied non-reacting gas flows using an open-source DSMC code

Rodrigo C. Palharini[1]

Instituto de Aeronáutica e Espaço, 12228-904 São José dos Campos, SP, Brazil

Craig White[2]

School of Engineering, University of Glasgow, Glasgow G12 8QQ, UK

Thomas J. Scanlon[3], Richard E. Brown[5]

Department of Mechanical & Aerospace Engineering, University of Strathclyde, Glasgow G1 1XJ, UK

Matthew K. Borg[4], Jason M. Reese[6]

School of Engineering, University of Edinburgh, Edinburgh EH9 3JL, UK

Abstract

Validation and verification represent an important element in the development of a computational code. The aim is establish both confidence in the algorithm and its suitability for the intended purpose. In this paper, a direct simulation Monte Carlo solver, called *dsmcFoam*, is carefully investigated for its ability to solve low and high speed non-reacting gas flows in simple and complex geometries. The test cases are: flow over sharp and truncated flat plates, the Mars Pathfinder probe, a micro-channel with heated internal steps, and a simple micro-channel. For all the cases investigated, *dsmcFoam* demonstrates very good agreement with experimental and numerical data available in the literature.

Keywords: DSMC, Benchmark, Open-source, Rarefied gas dynamics, Aerodynamics, Low/high speed flows.

[1]Postdoctoral Research Fellow, Division of Aerodynamics.
[2]Lecturer, University of Glasgow.
[3]Senior Lecturer, James Weir Fluids Laboratory.
[4]Professor, Centre for Future Air-Space Transportation Technology.
[5]Lecturer in Mechanical Engineering.
[6]Regius Professor of Engineering, School of Engineering.

1. Introduction

The accuracy and reliability of computer predictions is the focus of much study and debate in the fluid dynamics community. Computational codes can only be considered reliable if they pass a through rigorous process of verification and validation (V&V). In an effort to standardize the V&V process, a significant amount of literature has been produced on the subject, e.g., [1–8]. The present study adopts the V&V definition stated in Ref. [5], i.e.,

Verification: the process of determining that an implemented model is capable of correctly performing the task it was designed for.

Validation: the process of determining the degree to which a model is an accurate representation of the real world from the perspective of the intended use of the model.

In other words, verification deals with mathematics and numerics; the conceptual model that relates to the real world is not an issue. Validation deals with the actual physics and addresses the accuracy of the conceptual model with respect to the real world, i.e., as measured experimentally [4, 6].

In this paper, high and low speed inert gas flows are investigated in simple and complex geometries using the direct simulation Monte Carlo (DSMC) method [9]. DSMC is the dominant computational technique for numerical investigations of gas flows that fall within the transition-continuum Knudsen number (Kn) range; where

$$Kn = \frac{\lambda}{L}, \tag{1}$$

and λ is the mean free path of the gas, and L is a characteristic length scale of the system. When the Knudsen number is small ($Kn < 0.01$), non-equilibrium effects are insignificant and the standard Navier-Stokes-Fourier (NSF) equations can accurately predict the gas behavior. As Kn increases ($0.01 < Kn < 0.1$), regions of non-equilibrium begin to appear near surfaces as the molecule-surface interaction frequency is reduced; the most recognizable effect of this is velocity

slip and temperature jump, and the NSF equations with slip and jump boundary conditions can still be used effectively. However, once the Knudsen number increases into the transition-continuum ($0.1 < Kn < 10$) and free-molecular ($Kn > 10$) regimes, the NSF equations cannot predict the gas behavior. Recourse to solutions of the Boltzmann equation must be made, and DSMC has proven to be the most reliable method for this purpose in the transition regime, where non-equilibrium effects dominate the gas behavior but inter-molecular collisions are still important. Different forms of Knudsen number can be required to predict different types of continuum breakdown, e.g., a Knudsen number based on local flow gradient lengths can be used across shock waves [10–12].

This paper is intended to be an extension of the DSMC code and results published by Scanlon *et al.* [13], and demonstrates new developments and capabilities of the *dsmcFoam* code.

2. Code development and new features

DSMC is a stochastic particle-based method that provides a solution to the Boltzmann equation by emulating the physics of a real gas. A discrete set of simulator particles are tracked in time and space as they interact with each other and the boundaries of the simulation domain. Particle movements are handled deterministically according to the local time step and their velocity vectors. Once all movements have been completed, inter-molecular collisions are calculated in a stochastic manner in numerical cells. The first key assumption of the method is that a single DSMC simulator particle can represent any number of real atoms or molecules. This can drastically reduce the computational expense of a simulation. Second, it is assumed that particle movements and collisions can be decoupled, which increases the allowable time-step size by several orders of magnitude in comparison with fully-deterministic particle methods, such as molecular dynamics.

The *dsmcFoam* code is employed in the current paper to solve rarefied non-reacting gas flows over flat plates, the aerothermodynamics of the Mars

Pathfinder probe, and pressure-driven flow in micro-channels. This new freeware, based on Bird's algorithms, has been developed within the framework of the open-source computational fluid dynamics toolbox OpenFOAM [14], in conjunction with researchers at the University of Strathclyde, as described in Ref. [13]. Recent *dsmcFoam* code improvements [15, 16] not described in Ref. [13] include: a robust measurement framework, vibrational molecular energy, the quantum-kinetic (QK) chemistry model [17], and new boundary conditions, such as implicit, prescribed pressure inlets and outlets for low speed flows [18].

3. Code sensitivity

The accuracy of a DSMC simulation relies principally on four main constraints: (i) the computational cell size must be smaller than the local mean free path if possible collision partners are restricted to a particle's current cell, which is the case in *dsmcFoam*; (ii) the simulation time step must be chosen so that particles only cross a fraction of the average cell length in each time step, and the time step must also be smaller than the local mean collision time; (iii) the number of particles per cell must be large enough to preserve collision statistics; and (iv) the statistical scatter is determined by the number of samples, and for steady state problems sampling must not be started until a sufficient transient period has elapsed.

In this section we examine whether the DSMC requirements described above are rigorously respected. For this purpose, rarefied flow over a zero-thickness flat plate was chosen as a test case.

The freestream conditions are the same to those investigated by Lengrand *et al.* [19]. In this experimental study, a sharp flat plate of 0.1 m streamwise length and 0.1 m width was positioned at a distance from a nozzle producing a nitrogen flow with a freestream Mach number of 20.2, temperature of 13.32 K and pressure of 6.831×10^{-2} N/m^2.

In the computational solution, the geometry was constructed as a 3D flat plate, 0.1 m long and 0.1 m wide, positioned 0.005 m downstream of the uniform nitrogen stream that is parallel to the plate itself. Further details of the freestream conditions are given in Table 1. Based on these properties, and considering the flat-plate length as the characteristic length, the Knudsen number (Kn_L) and Reynolds number (Re_L) were 0.0235 and 2790, respectively.

Table 1: Freestream conditions for flat-plate simulations.

Parameter	**Value**	**Unit**
Velocity (V_∞)	1503	m/s
Temperature (T_∞)	13.32	K
Number density (n_∞)	3.719×10^{20}	m^{-3}
Density (ρ_∞)	1.729×10^{-5}	$\mathrm{kg/m}^3$
Pressure (p_∞)	6.831×10^{-2}	Pa
Dynamic viscosity (μ_∞)	9.314×10^{-7}	$\mathrm{N.s/m}^2$
Mean free path (λ_∞)	2.350×10^{-3}	m
Overall Knudsen (Kn_{L_p})	0.0235	
Overall Reynolds (Re_{L_p})	2790	

The computational domain used for the calculation was made large enough such that flow disturbances did not reach the upstream and side boundaries, where freestream conditions were specified. A schematic of the computational domain and boundary conditions is given in Fig. 1. Side I-A represents the flat-plate surface, and diffuse reflection with complete thermal accommodation to the surface temperature is the boundary condition applied to this surface. Side I-B represents a plane of symmetry. Sides II and III are boundaries with the specified freestream conditions; particles crossing into the computational domain are generated at these boundaries. Finally, side IV is defined as a vacuum boundary condition; the option for vacuum is suitable for an outflowing gas as there are no particles moving upstream if the Mach number is greater than 3.0 [9].

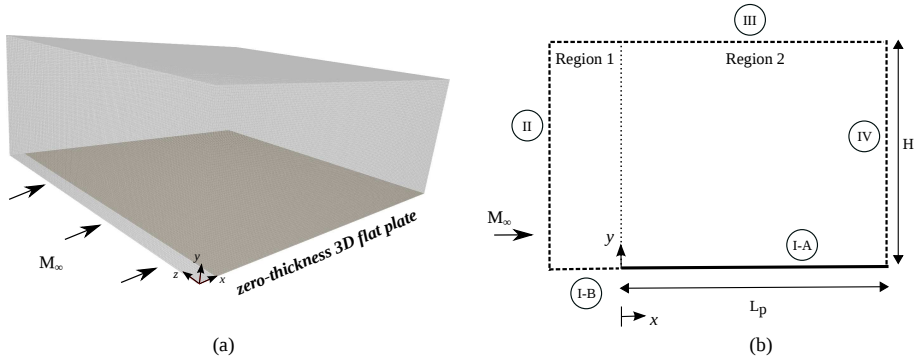

Figure 1: (a) 3D flat plate computational domain, and (b) specified boundary conditions.

In order to examine the effect of the grid resolution on the wall heat transfer and pressure coefficients, a set of simulations using standard, fine, and coarse meshes were performed. Grid independence was investigated by performing calculations for different numbers of cells in the x- and y-directions, and then comparing with a solution calculated on the standard grid. Figure 1 shows the standard computational domain which was divided into two regions. Region 1 consists of 10 cells along side I-B and 80 cells along side II, while region 2 consists of 200 cells distributed along side I-A and 80 cells normal to the plate surface, i.e., along side IV. In this way, the effect of altering the cell size in the x-direction may be analyzed for coarse and fine grids by halving or doubling the number of cells with respect to the standard grid, while the number of cells in the y-direction is kept constant. The same procedure is adopted for the y-direction, i.e., the cell size is altered keeping the number of cells in the x-direction constant. According to Figure 2(a), the grid sensitivity analysis shows good agreement for the three mesh sizes investigated indicating that the results were essentially grid-independent.

In a similar manner to the grid independence study, the influence of the time step size on the aerodynamic properties was examined. The time step is chosen to be smaller than both the mean collision time (MCT) and the cell residence time (Δt_{res}), with the latter being the time taken by a DSMC particle to cross a typical computational cell in freestream conditions. Based on these conditions,

the reference time step (Δt_{ref}) was set to be 6.28×10^{-8} s. Then, two time steps different from the Δt_{ref} were investigated $(\Delta t_{ref})/4$ and $(\Delta t_{ref})\times 4$. As shown in Fig. 2(b), the resulting simulations are essentially independent of the time step size, so long as the time step and cell size requirements are respected, in conjunction with the other good DSMC practice conditions described above.

In DSMC simulations the intermolecular collisions are the principal driver in the flow-field development. These intermolecular collisions occur in each cell, and sufficient particles should be employed not only to reduce the statistical error during the sampling process, but also to ensure the accuracy of the simulated collision rate. However, the use of a large number of particles greatly increases the computational effort. The balance between computational expense and accuracy has been studied by many authors [20–23], and 30-40 particles per cell is commonly employed [24–28]. However, there are some DSMC simulations [29, 30] that employed as few as 10 particles per cell, and some computations [31] as many as 50 to 120. The number of particles required is heavily influenced by the choice of collision model, and it is well-known that the majorant frequency scheme can use fewer particles than the no time-counter-method (NTC). Recent work has focused on reducing the number of particles required even further [32] using novel collision partner selection schemes. *dsmcFoam* uses the NTC method, so requires a reasonably large number of particles in order to recover the collision statistics.

In order to clarify this issue, we executed an additional study to consider the influence of the number of simulated particles on the *dsmcFoam* solution of a hypersonic flow over a flat plate. Considering that the standard mesh corresponded to a total of 43.7 million particles (or 13 particles per cell on average), two new cases were investigated using the same mesh. These cases corresponded, on average, to 21.8 and 87.4 million particles in the entire computational domain. The effects of such variations on the heat transfer and pressure are shown in Fig. 2(c). According to these results, the standard grid with a total of 43.7 million particles is considered sufficient for the present computations.

The accuracy of the DSMC method may also be influenced by the number

of time steps that results are sampled over (N_s) [24–30]. Since the macroscopic properties of the flow are obtained by sampling all particles within a cell, the number of samples must be sufficient to minimize the statistical error. The magnitude of the statistical error reduces with the square root of the sample size, and it is important to determine the value of N_s that provides acceptable data scattering. For this purpose, the standard grid with approximately 43.7 million particles was run for 50,000, 100,000, 200,000, and 300,000 sampling time steps. Figure 2(d) shows very good agreement across the range of number of samples considered. Based on these plots, an N_s of 300,000 was considered as providing an acceptable fluctuation level for the case investigated.

In this section, hypersonic non-reacting gas flow simulations over a zero thickness flat plate were performed. Grid spacing, time step size, number of particles per cell, and number of computational samples were examined in order to test that the assumptions adopted as standard would lead to results independent of the grid, time step and number of statistical samples. On examining these results, no appreciable changes were observed; however, altering the parameters mentioned above, significantly impacted on the computational efficiency of the simulations. In the next section, we adopted the standard procedure for all of the simulations, and the results obtained using *dsmcFoam* are compared to other numerical and experimental data.

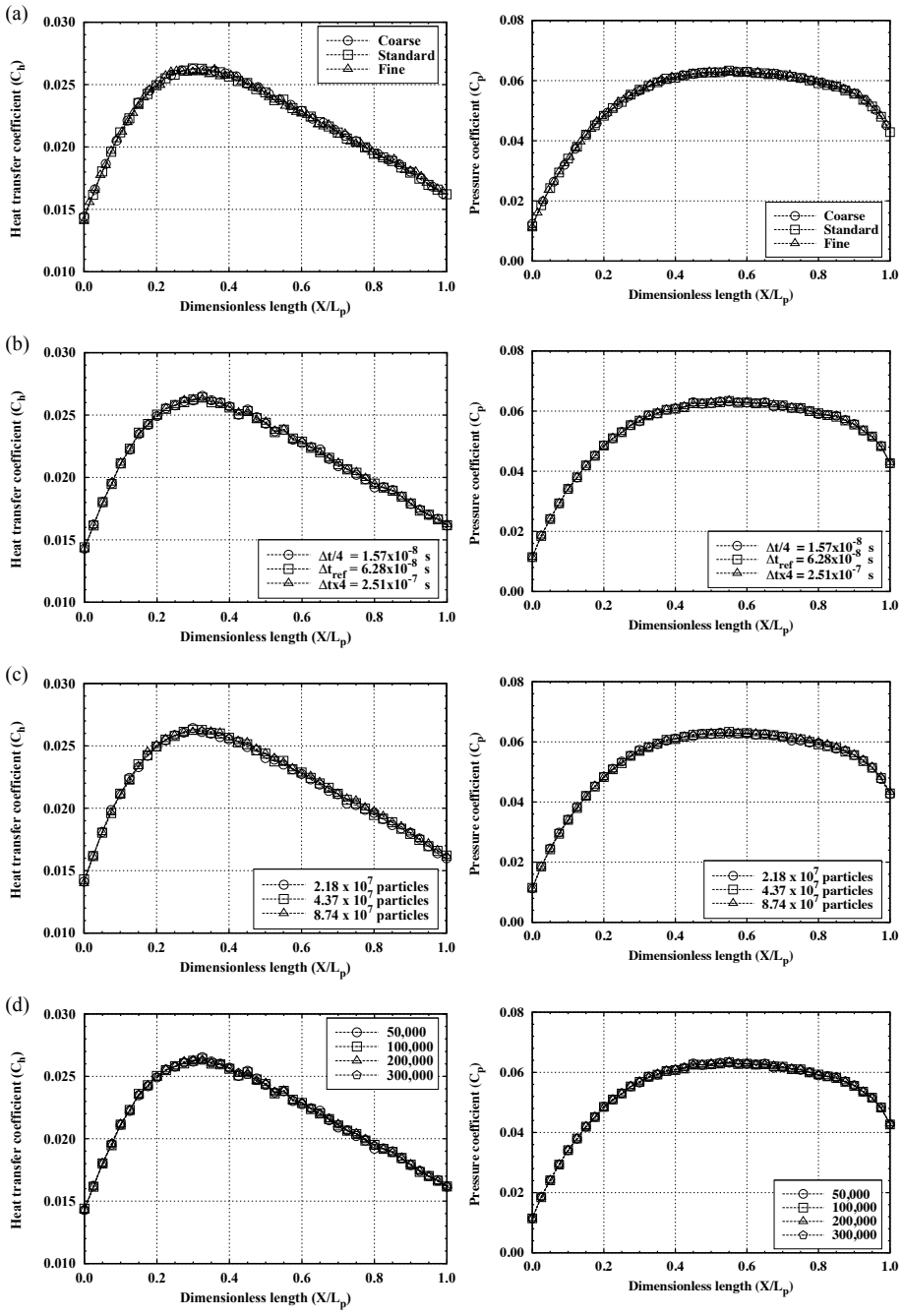

Figure 2: (a) Effect of varying the number of cells, (b) the time step, (c) the number of samples, and (d) number of DSMC particles per cell on the heat transfer (left column) and pressure (right column) coefficients in the zero-thickness flat-plate case.

4. Benchmark test cases for *dsmcFoam*

The validation strategy consists of comparing the results obtained using *dsmcFoam* with other numerical, analytical, or experimental results available in the literature. In the following sections, the validation process for *dsmcFoam* is discussed in detail.

4.1. Benchmark Case A: Flow over sharp and truncated flat plates

Rarefied hypersonic flow over flat plates has been studied theoretically, experimentally, and numerically by many authors, e.g., [33–40]. The extremely simple geometry makes the flat plate one of the most useful test cases for numerical validation purposes.

The test cases we choose to validate *dsmcFoam* for non-reacting flows are based on the experimental-numerical study conducted by Lengrand *et al.* [19] and Allègre *et al.* [37]. In their experimental work, sharp and truncated flat plates of 0.1 m length (L_p), 0.1 m width (W_p), and 0.005 m thick (T_p) were positioned in a flow of nitrogen at two angles of incidence, 0° and 10°. The physical model was supplied with an internal water cooling system which maintained the wall temperature at 290 K. Wall pressure and heat flux measurements were made by placing pressure transducers and chromel-alumel (Ch/Al) thermocouples along the longitudinal symmetry axis of the flat plates. In addition, density flowfield measurements were carried out by employing an electron beam fluorescent technique. The uncertainties in the experimental pressure, heat flux and density measurements were estimated to be 15%, 10%, and 10%, respectively.

In addition to the experimental work, numerical simulations were performed using the NSF equations [19, 37] and the DSMC method [19, 37, 39]. The NSF results were obtained at ONERA using an implicit finite-volume method taking into account velocity slip and temperature jump at the wall. The DSMC in-house code were developed by the Laboratoire d'Aérothermique of the Centre National de la Recherche Scientifique (CNRS) [19] and the Institute of Space and Aeronautical Science (ISAS) [39]. In the DSMC computations performed

by Lengrand *et al.* [19], vibrational molecular energy was neglected and the Larsen-Borgnakke model [41] was employed for rotational-translational energy exchange. Particle collisions and collision sampling were performed using the variable hard sphere (VHS) model and the time-counter technique (TC) [9], respectively. However, the diatomic molecular collision (DMC) model [42] and the null-collision technique (NCT) [43] were adopted by Tsuboi *et al.* [39]. Since the data and assumptions employed in each method are available in the literature, the discussions below are limited only to details considered necessary.

In order to validate *dsmcFoam*, 3D sharp and truncated flat plates, as illustrated in Fig. 3, with the same dimensions as in Lengrand *et al.* [19] and Allègre *et al.* [37], were modeled. In the present computational solution, the two plates were immersed in nitrogen gas with an inlet imposed 0.005 m upstream of the plate. The freestream conditions (Table 1) and the computational domains are similar to those presented in Section 3. The computational mesh was composed of 4.7 million and 3.4 million cells for the sharp and truncated cases, respectively. On average, 13 DSMC particles per cell were employed in the simulations; the VHS collision model was applied, and the energy exchange between the translational and rotational modes was modeled using the Larsen-Borgnakke algorithm [41]. The NTC [44] technique was used to control the molecular collision sampling. The value of rotational collision number (Z_{rot}) was set to be 1 for the sharp plate to match that used by Lengrand *et al.* [19]. No information for Z_{rot} in the truncated flat-plate case was given by Allègre *et al.* [37], therefore we used $Z_{rot} = 1$ and $Z_{rot} = 5$ to compare with their results. Additional simulation parameters are given in Table 2.

The resulting normalized density (ρ/ρ_∞) contours for zero-thickness, sharp, and truncated flat plates are shown in Fig. 4, compared with other numerical and experimental results. Despite the different energy redistribution models and collision techniques used in each of the simulations, a very good qualitative agreement is evident between the *dsmcFoam* results and the numerical and experimental studies presented by Allègre *et al.* [37] and Tsuboi *et al.* [39].

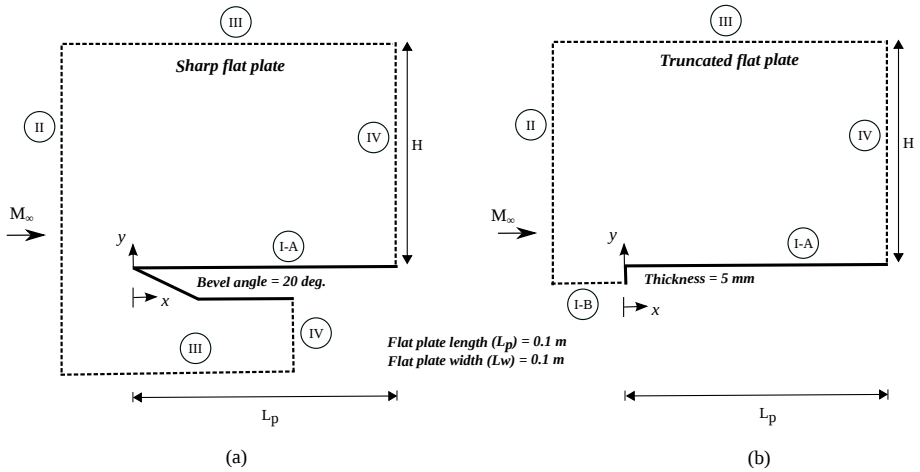

Figure 3: 2D schematic of sharp (a) and truncated (b) flat plates.

Table 2: Numerical parameters for the flat-plate simulations.

Parameters	Z_{rot}	ω	d_{ref} [m]	Δt [s]	MCT [s]	λ_∞ [m]
Sharp	1	0.74	4.17×10^{-10}	6.28×10^{-8}	1.90×10^{-5}	3.35×10^{-3}
Truncated	1 and 5	0.74	4.17×10^{-10}	6.28×10^{-8}	1.90×10^{-5}	3.35×10^{-3}

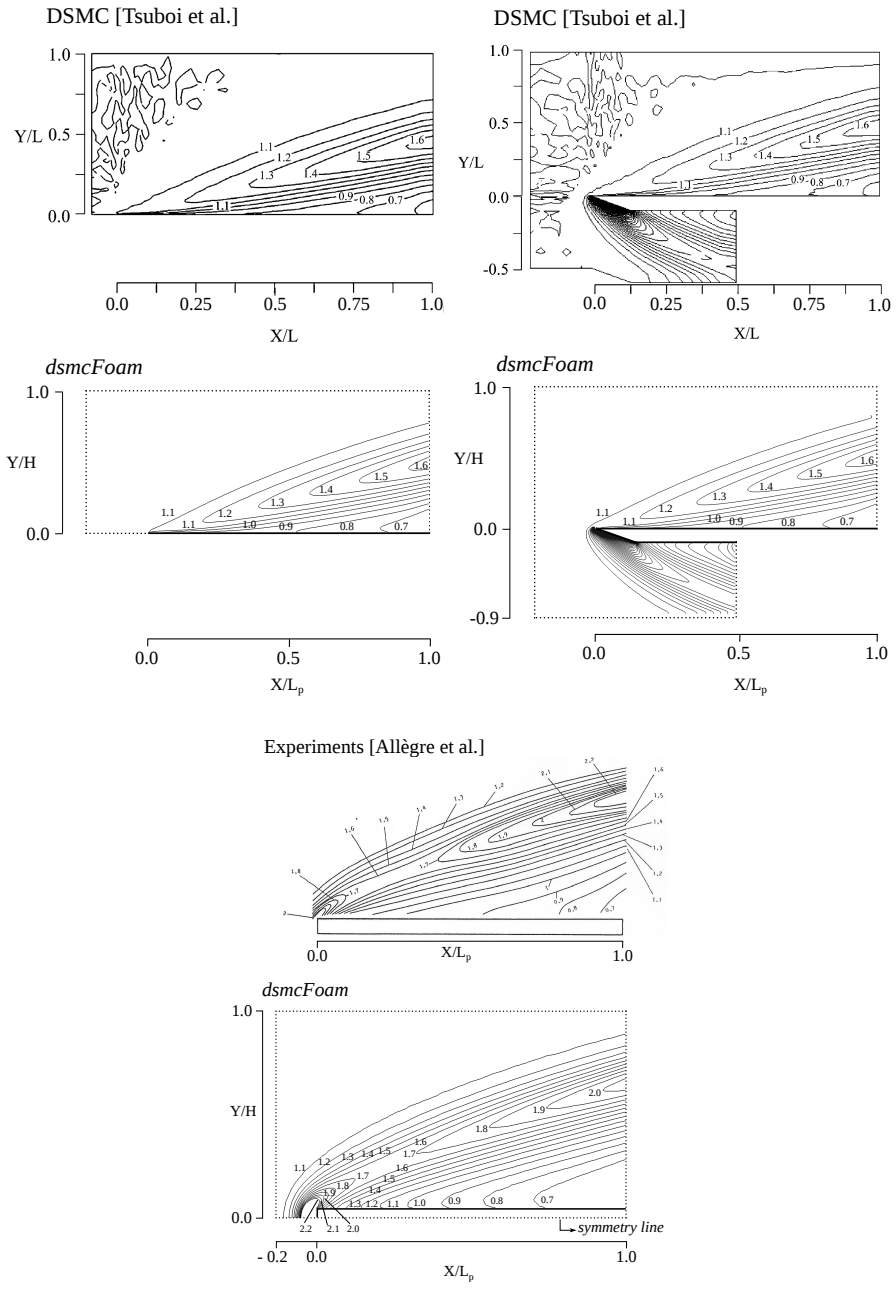

Figure 4: Density ratio (ρ/ρ_∞) contours around zero thickness (top left), sharp (top right), and truncated (bottom) flat plates.

The normalized density (ρ/ρ_∞) and temperature (T/T_∞) distributions normal to the sharp flat-plate surface at the non-dimensional streamwise location $X/L_p = 0.75$ are shown in Fig. 5. Good agreement is found between the DSMC calculation and the experimental results. The density peak is captured well by the present simulation, and the normalized density profile follows the same trend of the numerical and experimental results performed by Tsuboi *et al.* [39] and Lengrand *et al.* [19], respectively. The NSF simulations of Lengrand *et al.* [19] were not able to predict correctly the density profile at the position considered.

Analyzing the translational and rotational temperature profiles in Fig. 5(b), a difference between the rotational and translational temperatures is observed, which indicates thermally non-equilibrium conditions. The normalized temperature is low close to the surface, increases to a maximum value inside the shock layer at $Y = 0.05$ and then declines to the freestream temperature at the upper boundary condition. In general, there is very close agreement of translational and rotational temperature profiles from *dsmcFoam* and the CNRS DSMC code [19].

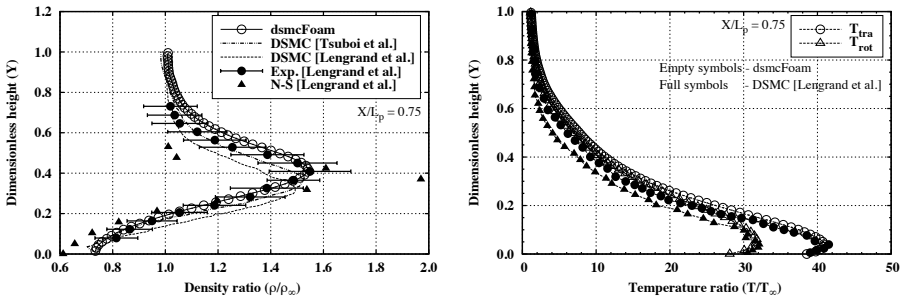

(a) (b)

Figure 5: (a) Normalized density (ρ/ρ_∞) and (b) normalized temperature (T/T_∞) profiles normal to the sharp flat plate at streamwise position $X/L_p = 0.75$.

Figure 6 shows the heat transfer (C_h), pressure (C_p) and skin friction (C_f) coefficients along the flat plates. For the sharp flat plate case (left column) the comparison of the *dsmcFoam* results with the experimental data is better than than found by Lengrand *et al.* [19] and Tsuboi *et al.* [39]. The skin friction coefficient shows good agreement with the Lengrand *et al.* [19] DSMC results at the leading edge and from position $X/L_p \cong 0.4$ to 1.0. When the NSF calculations for C_h and C_p for a rarefied flow over a sharp flat plate are compared with experimental and DSMC results, it is clear that the CNRS NSF simulations were unable to capture the surface quantities for the conditions investigated.

According to Lengrand *et al.* [19], possible sources of experimental error are related to uncertainties in the freestream conditions, measurement procedures, and the influence of the leading edge bluntness or bevel angle. In order to investigate the impact of the leading edge bluntness, Fig. 6 (right column) shows comparisons of the *dsmcFoam* results with experimental data from Allègre *et al.* [37] and previous DSMC simulations. From the heat transfer (C_h) plot, excellent agreement is seen between the DSMC simulations apart from at the leading edge ($X/L_p = 0$) where the *dsmcFoam* results do not tend to zero. Both computations demonstrated significant difference when compared with experimental data.

In contrast with C_h results, the pressure coefficient (C_p) shows very good agreement between numerical and experimental data. However, the numerical results show slightly higher values for C_p at the flat-plate leading edge. For the skin friction coefficient along the truncated flat plate, no numerical results were available in the literature. Since the value of Z_{rot} was not specified in Ref. [37], *dsmcFoam* computations for rarefied gas flow over the truncated flat plate were performed with $Z_{rot} = 1$ and 5; however, no significant differences in the surface quantities were observed.

In summary, hypersonic non-reacting gas flow over three-dimensional zero-thickness, sharp, and truncated flat plates was simulated using *dsmcFoam*. Excellent agreement between numerical and experimental data for the density contours was found. The results also demonstrated that the shape of the leading

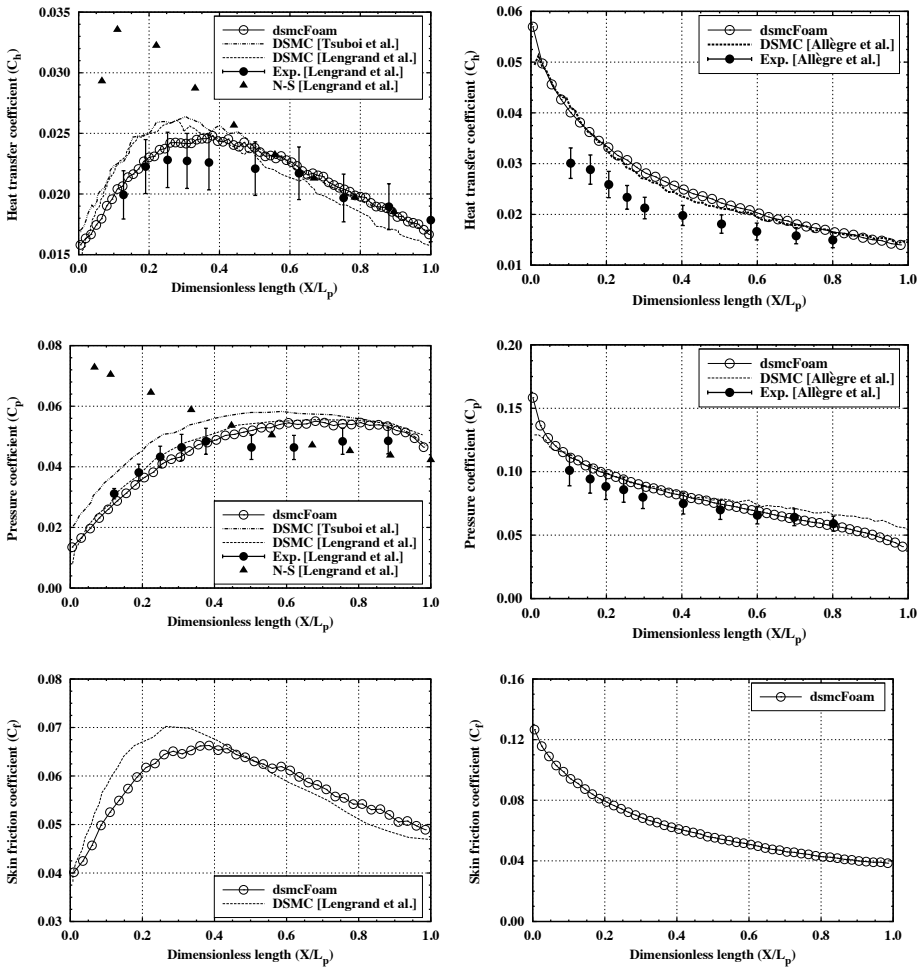

Figure 6: Comparisons of heat transfer (C_h), pressure (C_p), and skin friction coefficients (C_f) from *dsmcFoam* simulations and independent numerical/experimental data for sharp (left) and truncated (right) flat plates.

edge can affect the flow and shock structure over the plate. For the aerodynamic properties on a sharp flat plate, satisfactory agreement was found from the leading edge up to $X/L_p = 0.2$; however, certain discrepancies were observed further along the plate. In contrast, the truncated case exhibited differences between the numerical and experimental data in the leading edge region, while better agreement was evident towards the trailing edge. Comparisons between the

DSMC and NSF results demonstrate that the continuum approach, even when using slip velocity and temperature jump boundary conditions, cannot be used with confidence to predict these types of thermodynamically non-equilibrium flows.

4.2. Benchmark Case B: Flow over a 70° blunted cone

The flow over blunt bodies at high speeds and high altitudes displays complex flow interactions, and requires a precise determination of the heating rate, aerodynamic forces, and the flowfield surrounding the body. The characterization of the wake region is also a key factor for the success of re-entry missions.

In an experimental set-up, a 70° blunted cone, identical in geometric proportions to that of the Mars Pathfinder probe, was chosen by the AGARD Working Group 18 [45]. Rarefied flow experiments were performed in five different facilities: the SR3 wind tunnel at CNRS-Meudom, the V2G, V3G and HEG wind tunnels at DRL-Göttingen, and the LENS wind tunnel at the Buffalo Research Center (Calspan, University of Buffalo, USA). The experimental test conditions used in each of these experimental facilities are available in Ref. [45].

Allègre *et al.* [46–48] provided detailed information regarding experiments conducted at CNRS-Meudon. The CNRS group employed three freestream flow conditions, representative of different levels of rarefaction, and three probe models, each one having a base and afterbody sting diameter of 0.05 and 0.0125 m, respectively.

The CNRS model utilized for the flowfield density measurements was made of brass, water cooled, with a wall temperature remaining close to 290 K during all measurements. An electron beam fluorescent technique was used to measure the density field around the blunted cone [46]. For the aerodynamic force measurements, the model was made of aluminum, uncooled, with the wall temperature estimated to be close to 350 K. The model was directly attached to an external balance providing direct measurements of drag, lift, and pitching moment, and indirect determinations of the center of pressure at different angles of attack [47]. For heat transfer measurements, a steel model was used

in which the wall temperature was kept close to 300 K [48]. Chrome-alumel (Ch/Al) thermocouples were embedded through the wall thickness at nine locations along the forebody, base plane, and sting, and the thin-wall technique was applied to measure the heat fluxes on the steel probe.

An extensive set of simulations at these experimental test conditions were completed using both DSMC [49–58] and Navier-Stokes [59–62] methods prior to the release of the experimental data. In this way, it was possible to perform a blind validation test of the computational codes.

In the present work, the simulated freestream conditions are the same as those used in the SR3 low-density wind tunnel (case 1) [46–48]. The Mars Pathfinder probe was immersed in a non-reacting uniform nitrogen flow of velocity, mass density, and temperature equal to 13.316 m/s, 1.73×10^{-5} kg/m^3, and 13.316 K, respectively. Energy exchange was allowed between the translational and rotational modes and was controlled by the Larsen-Borgnakke phenomenological model [41]. Molecular collisions were modeled using the variable hard sphere (VHS) model [63], and the no-time-counter (NTC) collision sampling technique [44]. In addition, simulation parameters for N_2 are: reference diameter (d_{ref}), rotational collision number (Z_{rot}) and viscosity index (ω) set equal to 4.17×10^{-10} m, 5, and 0.74, respectively [9].

Figure 7(a) shows the experimental model configuration and Fig 7(b) gives an amplified view of the *dsmcFoam* computational grid. The computational grid was composed of a mixture of 7.1 million hexa- and polyhedral cells with, on average, 10.5 simulated particles per cell. A uniform hexahedral mesh, with cell sizes smaller than the freestream mean free path, is used for most of the domain, with some polyhedral cells to capture the surface geometry. Each simulation was performed using 240 processors on the parallel machine at the University of Strathclyde, and 10 days were required to fully resolve each of the cases.

The computational domain was large enough so that the upstream, downstream, and upper boundary conditions could be specified as freestream. In order to minimize computational effort, quarter symmetry was employed for 0° angle of attack. Undisturbed freestream conditions were imposed 0.02 m

upstream of the probe, and the computational domain normal to the probe extended a distance 0.08 m in the y- and z-directions. The surface temperature was set at 290 K, 300 K, and 350 K for the density, heat transfer and aerodynamic force measurements, respectively. The surface boundary condition assumed the gas-surface interaction to be diffuse, with full thermal accommodation at the specified surface temperature.

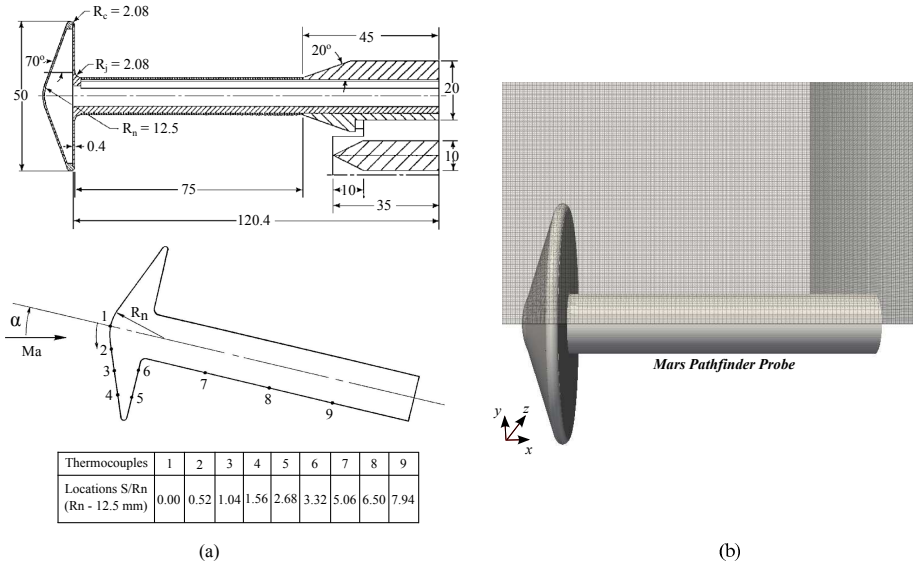

Thermocouples	1	2	3	4	5	6	7	8	9
Locations S/Rn (Rn - 12.5 mm)	0.00	0.52	1.04	1.56	2.68	3.32	5.06	6.50	7.94

(a) (b)

Figure 7: (a) Experimental 70° blunted cone model for heat transfer measurements with thermocouple locations from [48], and (b) schematic of the corresponding *dsmcFoam* 3D computational mesh.

In Fig. 8 experimental density flowfields at different angles of attack [46] are compared with the results from the *dsmcFoam* calculations. Qualitatively, the results show a good level of agreement between the experimental and *dsmcFoam* results. According to Allègre *et al.* [46] the flowfield density measurement accuracy is estimated to be 10%, except in the region encompassing the forward shock wave, which is characterized by high density gradients and has a higher uncertainty.

Comparison is also made with the DAC (DSMC Analysis Code) simulations, developed at the NASA Johnson Space Flight Center [64] and available

in Ref. [49]. In Fig. 9, excellent agreement of the density ratio (ρ/ρ_∞), overall temperature (T_{ov}), and Mach number (M) contours at 0° degree angle of attack is found between the codes; where

$$T_{ov} = \frac{T_{trans}\xi_{trans} + T_{rot}\xi_{rot}}{\xi_{trans} + \xi_{rot}}, \tag{2}$$

with T_{trans} and T_{rot} the translational and rotational temperatures of the gas, respectively, and ξ_{trans} and ξ_{rot} the number of degrees of freedom in the translational and rotational modes, respectively.

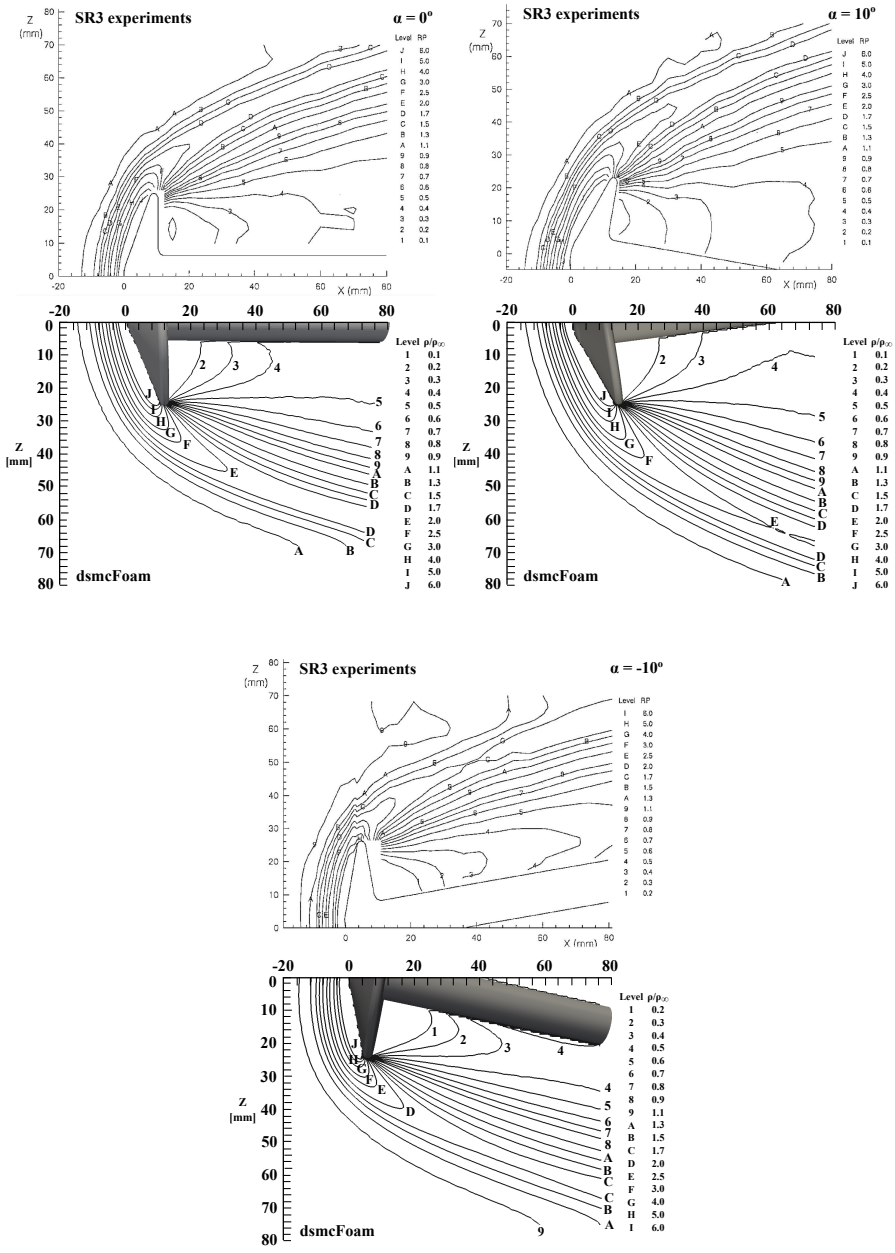

Figure 8: Density ratio (ρ/ρ_∞) distributions from *dsmcFoam*, and from the SR3 experiments [46] at different angles of attack (α), and Mach number 20.2.

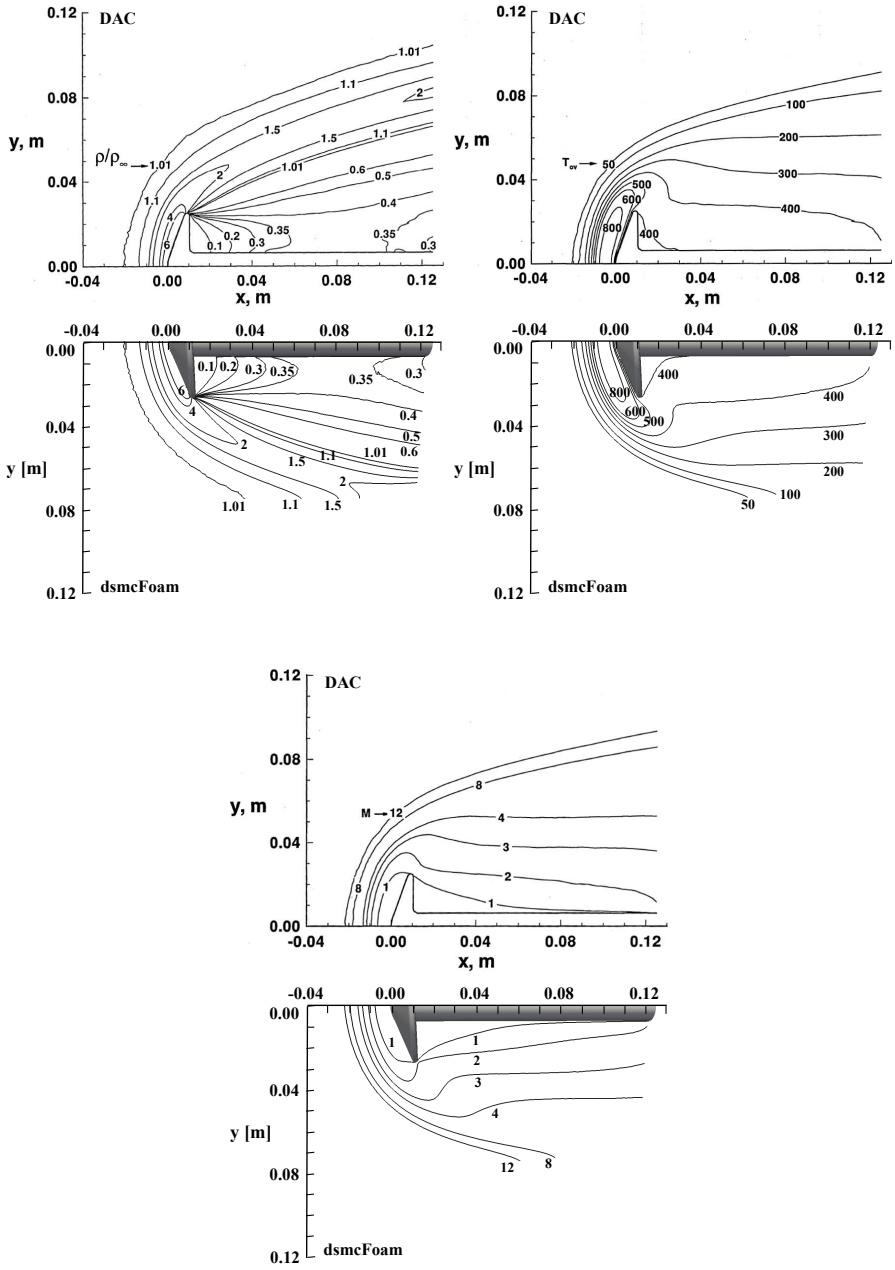

Figure 9: (top left) Density ratio (ρ/ρ_∞), (top right) overall temperature (T_{ov}), and (bottom) Mach number (M) distributions from *dsmcFoam* and from the DAC simulations [49] at 0° degree of attack, and Mach number 20.2.

The aerodynamic forces and moments have also been experimentally and numerically investigated [47, 51, 53] for different angles of attack. In Figs. 10 and 11 a satisfactory concurrence is found between the experimental data and *dsmcFoam* simulations. According to Allègre *et al.* [47], the global uncertainty in the aerodynamic coefficients and forces did not exceed ±3%, and the maximum difference between measured and simulated results was 8.6% on the normal force at 30° angle of attack. Table 3 shows the drag and lift coefficients, and the axial and normal forces coefficients, from the experimental measurements and numerical predictions using the *dsmcFoam* code.

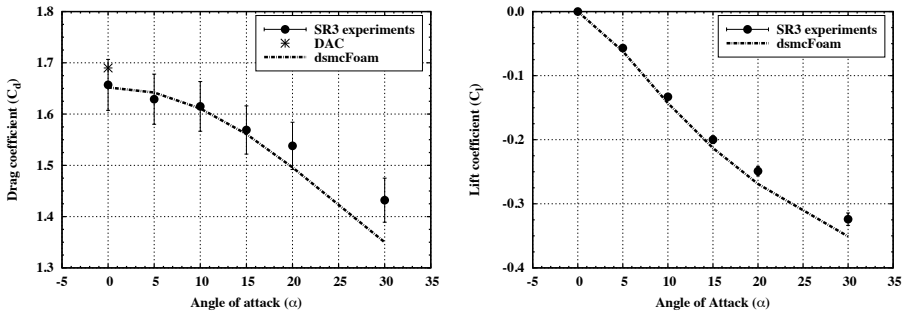

Figure 10: Drag (C_d) and lift (C_l) coefficients at different angles of attack (α).

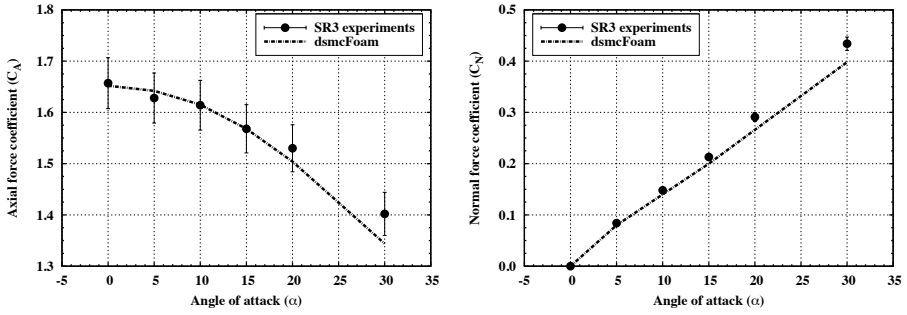

Figure 11: Axial (C_A) and normal (C_N) force coefficients at different angles of attack (α).

Table 3: Experimental and *dsmcFoam*-calculated aerodynamic and force coefficients.

Angle	Drag			Lift			Axial force			Normal force		
	exp.	calc.	% diff.	exp.	calc.	% diff.	exp.	calc.	% diff.	exp.	calc.	% diff.
0^o	1.657	1.652	0.302	0.000	0.000	0.000	1.657	1.652	-0.302	0.000	0.000	0.000
5^o	1.629	1.642	0.798	-0.057	-0.062	8.772	1.628	1.642	0.860	0.084	0.080	-4.762
10^o	1.615	1.611	-0.248	-0.133	-0.143	7.519	1.614	1.615	0.0620	0.148	0.140	-5.405
15^o	1.569	1.561	-0.510	-0.200	-0.213	6.500	1.568	1.568	0.000	0.213	0.200	-6.103
20^o	1.538	1.496	-2.731	-0.249	-0.269	8.032	1.530	1.504	-1.700	0.291	0.266	-8.591
30^o	1.432	1.350	-5.726	-0.324	-0.351	8.333	1.402	1.344	-4.137	0.434	0.398	-8.294

The effect of the angle of attack on the heat transfer (C_h) and pressure (C_p) coefficients is shown in Figs. 12 and 13. In this set of plots, the results are presented as a function of the normalized arc distance (s/R_n) measured from the forebody stagnation point to the end of the sting. Here, the *dsmcFoam* results are compared with DSMC computations provided from the DAC [50] and molecular gas dynamics simulator (MGDS) [40] codes, as well as with the experiments performed at the CNRS facilities [48].

According to Fig. 12, *dsmcFoam* shows a good agreement with DAC and MGDS for all angles of attack considered. The heat transfer coefficient is captured well by the numerical codes at the forebody and sting regions; however, a significant difference in C_h is seen between computations and experiments at the probe shoulder ($S/R_n \approx 2$). This difference is even higher when the angle of attack is increased, as shown in Fig. 14. At 30° angle of attack, the flow is compressed against the probe shoulder generating high heating rates in this region. Nevertheless, there is no thermocouple at this position; the last thermocouple on the forebody region is located at $S/R_n = 1.56$ but the simulated heat transfer peak occurs at $S/R_n \approx = 2.0$. For this reason, the peak in the heat transfer is not captured by the CNRS experiments. Even at locations where thermocouples are present, both *dsmcFoam* and MGDS predict higher heat fluxes than the experiments. Again, at 30° angle of attack, MGDS predicts a slightly lower heat flux at the stagnation point, compared to *dsmcFoam*. MGDS used a mesh refinement algorithm to ensure cells stay smaller than the local mean free path, whereas *dsmcFoam* uses a fixed grid, so the cells in the high density region near

the stagnation point may be larger than the local mean free path.

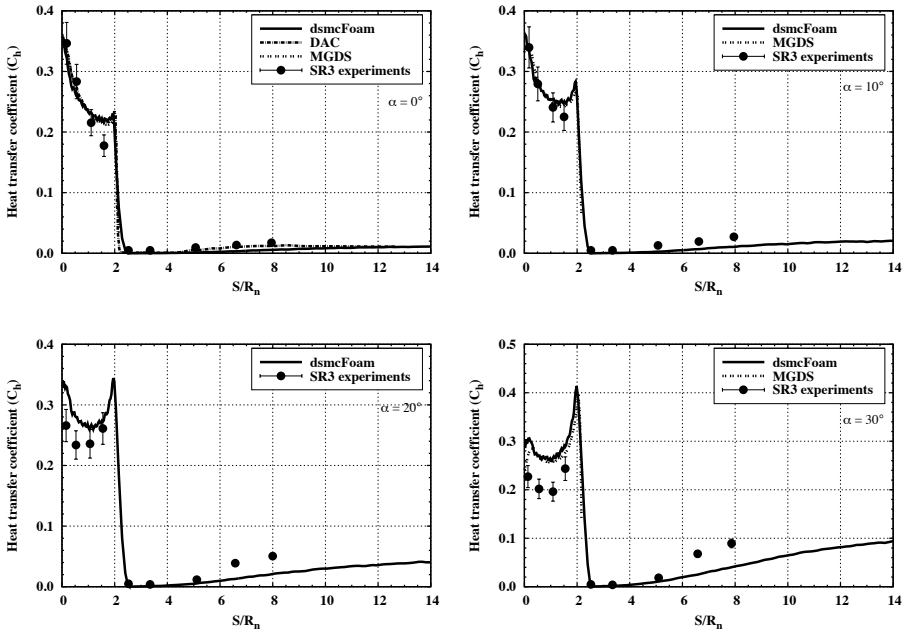

Figure 12: Heat transfer coefficients (C_h) along the Mars Pathfinder surface from *dsmcFoam*, DAC, MGDS and CNRS experiments at different angles of attack (α).

Figure 13 shows the pressure coefficient along the Mars Pathfinder probe surface. Excellent agreement is found between the *dsmcFoam* and DAC codes for 0° angle of attack. As the angle of attack is increased, the pressure coefficient increases at the probe shoulder, following the same trend as the heat transfer coefficient.

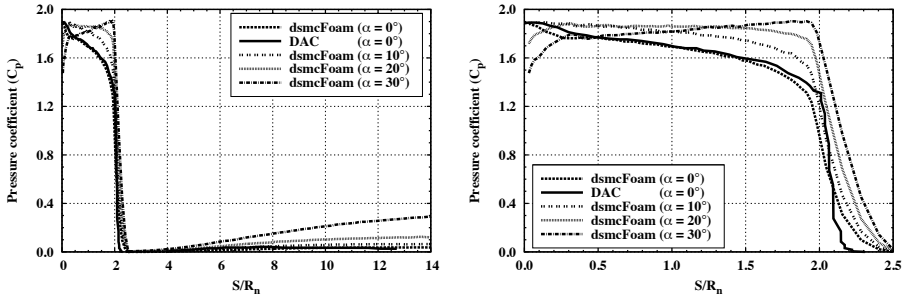

Figure 13: Pressure coefficient (C_p) along the Mars Pathfinder surface for *dsmcFoam* and DAC simulations at different angles of attack (α): full geometry (left), and forebody surface (right).

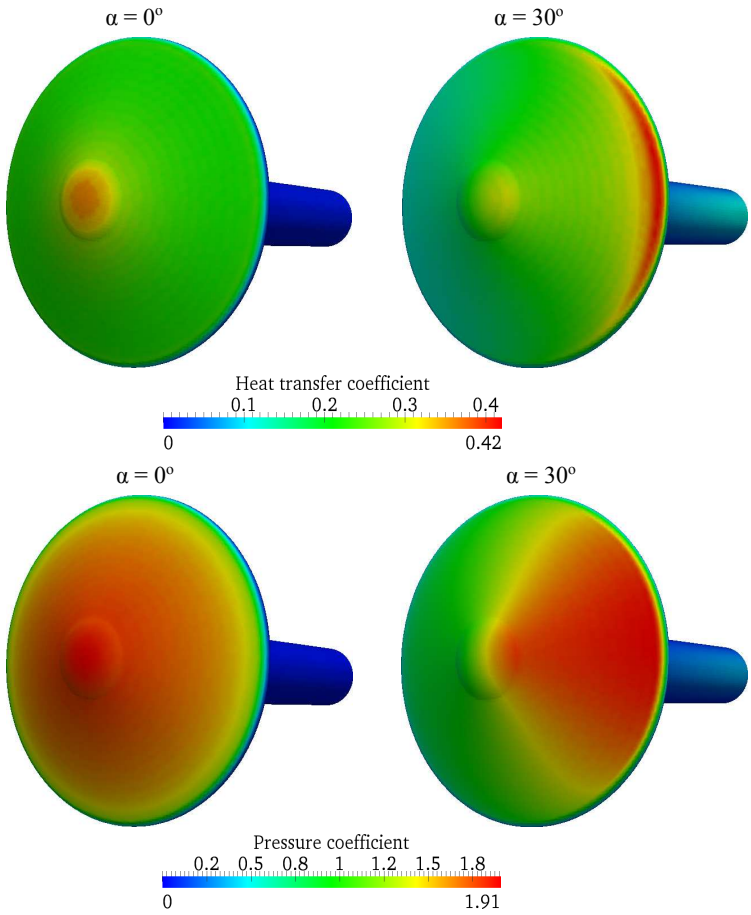

Figure 14: (top) Heat transfer (C_h) and (bottom) pressure (C_p) coefficient contours at 0^o (left) and 30^o (right) angles of attack (α), and Mach number 20.2.

When a probe enters a planetary atmosphere at high velocities, the forebody flowfield is dominated by a strong shock wave that causes the excitation, dissociation and possibly ionization of the gas surrounding the vehicle. This highly thermochemically non-equilibrium flow rapidly expands around the probe shoulder into the near wake region with a significant increase in rarefaction [49, 58, 65]. The flowfield complexity for the Mars Pathfinder probe is shown in Fig. 15(a). Due to this complexity, the aerothermodynamics of the wake may not be measured accurately; according to Wright and Milos [66] the uncertainty in the aeroheating measurements in this region is typically assumed to be in the range of 50-300%. This level of uncertainty plays a significant role in the vehicle design and the correct selection of a thermal protection system (TPS).

In order to compare the results obtained using the *dsmcFoam* code with those from DAC simulations provided by Moss *et al.* [49], normalised density, velocity, and temperature profiles are presented at four different locations in the probe afterbody region as depicted in Fig. 15(b).

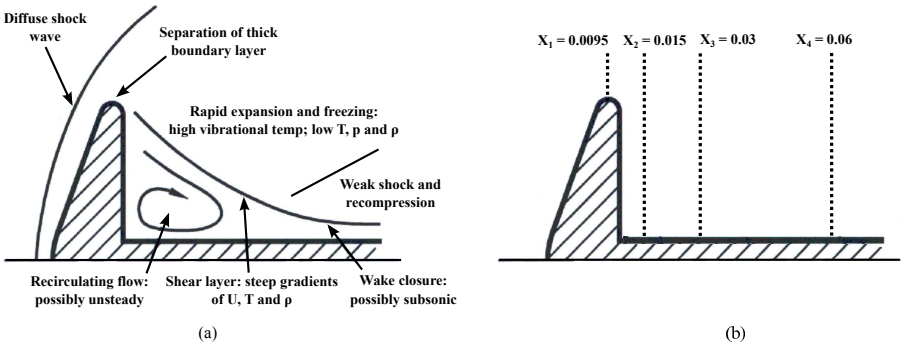

Figure 15: (a) Schematic of the planetary probe flow structure [58], and (b) macroscopic properties measurement locations.

From Figs. 16 to 18, it is clear that there is very good agreement between the DAC and *dsmcFoam* simulations. However, for the density and temperature profiles at location $X_1 = 0.0095$, some slight discordance is observed. In this region a very strong flow expansion occurs and the different mesh densities

between the two simulations may have some influence on the flowfield structure.

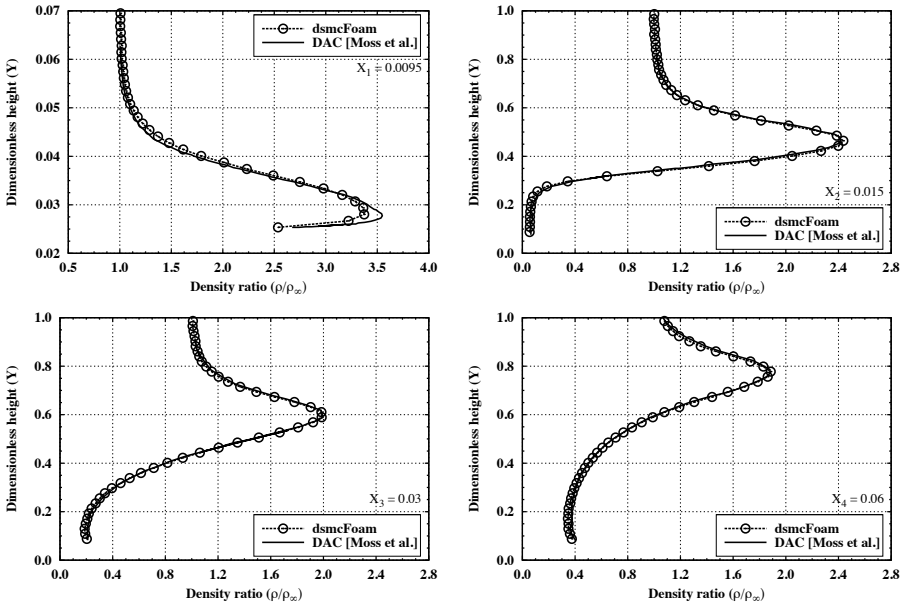

Figure 16: Density profiles (ρ/ρ_∞) computed by *dsmcFoam* and DAC.

To summarize this section, simulations have been performed using the *dsmcFoam* code for non-reacting flows over both flat plates and the Mars Pathfinder probe. The present data are compared with experimental and numerical solutions available in the open literature. Assuming the average uncertainty in the experimental data to be approximately 10% [19, 37, 46–48], a satisfactory level of agreement between the measurements and computations has been achieved.

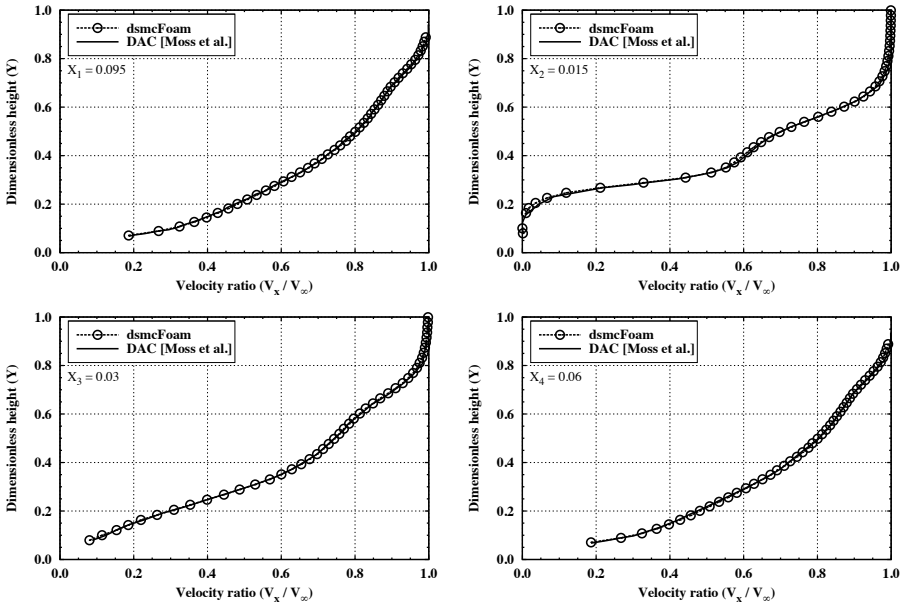

Figure 17: Velocity profiles (V_x/V_∞) computed by *dsmcFoam* and DAC.

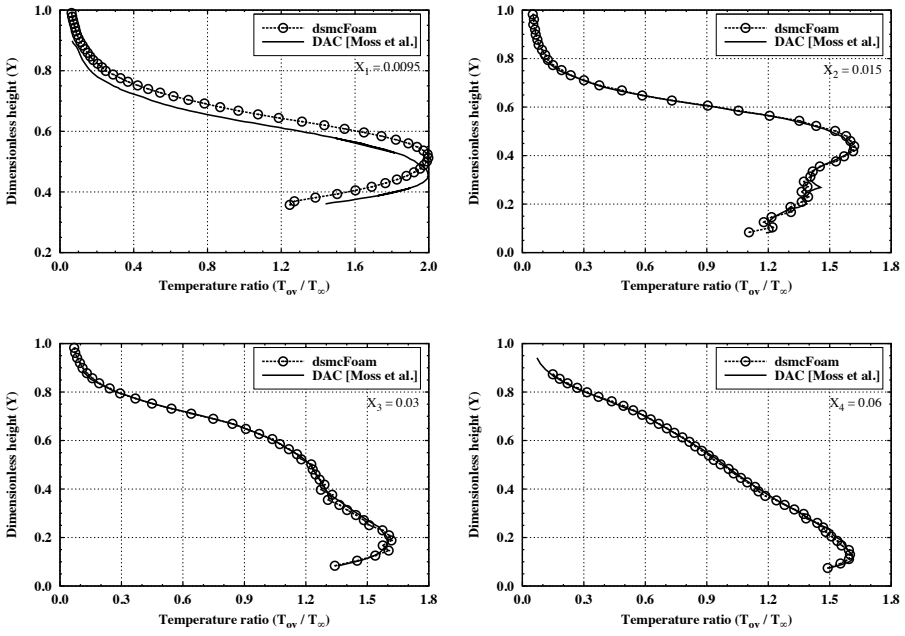

Figure 18: Temperature profiles (T_{ov}/T_∞) computed by *dsmcFoam* and DAC.

4.3. Benchmark Case C: flow in patterned 2D microchannels

The previous test cases have been for hypersonic flows, but progress has also been made in the extension of the *dsmcFoam* code to subsonic, pressure-driven flows in micro- or nano-scale geometries. In contrast to the previous cases where the Knudsen number is high because the gas density is low, micro-scale devices often operate in standard atmospheric conditions. The Knudsen number is high in these types of problems because the characteristic length scale L is small.

dsmcFoam has previously been benchmarked for planar Poiseuille flow with defined pressure inlets and outlets [67], where comparison to analytical solutions for the non-linear pressure profile were presented. The general starting point for the treatment of an inlet or outlet boundary condition in DSMC is to impose a particle flux. The rate of particle insertion, $\dot{N}$, can be computed from the equilibrium Maxwell-Boltzmann distribution, which requires boundary values of temperature, density, and velocity. The streaming velocity profiles for internal micro-scale flows at the inlet and outlet boundaries are generally not known *a priori*, so the boundary conditions described below use the theory of characteristics to calculate the local streaming velocity as the simulation proceeds.

Wang and Li [18] proposed an inlet boundary condition with target gas properties of pressure p_{in} and temperature T_{in}, prescribed at the inflow boundary. The perfect gas law is used to calculate the inlet number density n_{in},

$$n_{in} = \frac{p_{in}}{k_B T_{in}}. \tag{3}$$

Based on the theory of characteristics, the stream-wise u_{in} and tangential v_{in} velocities at two-dimensional inlet boundary faces f, using values from the boundary cell centres j, are calculated as

$$(u_{in})_f = u_j + \frac{p_{in} - p_j}{\rho_j a_j}, \tag{4}$$

and

$$(v_{in})_f = v_j, \tag{5}$$

where u_j and v_j are first order extrapolations from the cells attached to the relevant boundary face, ρ is mass density and a is the local speed of sound. The pressure p_j is calculated in these boundary conditions from the overall temperature as:

$$p_j = \rho_j R \left[\left(\frac{3T_{tr} + \bar{\zeta}_{rot} T_{rot}}{3 + \bar{\zeta}_{rot}} \right) \right]_j . \tag{6}$$

At the exit boundaries, only the pressure is defined and the boundary conditions are those first proposed by Nance *et al.* [68]:

$$(\rho_{out})_f = \rho_j + \frac{p_{out} - p_j}{(a_j)^2}, \tag{7}$$

$$(u_{out})_f = u_j + \frac{p_j - p_{out}}{\rho_j a_j}, \tag{8}$$

$$(v_{out})_f = v_j, \tag{9}$$

$$(T_{out})_f = p_{out} / \left[R (\rho_{out})_f \right] . \tag{10}$$

The pressure p_j is again calculated from Eq. (6). The process for selecting the required translational and rotational energies for particles at the boundaries is standard in DSMC, and details can be found in Ref. [9].

Here, we investigate a pressure-driven flow through a micro-channel with two heated steps on its lower surface, as shown in Fig. 19, which was first considered using DSMC by Fang and Liou [69]. The inlet pressure is 0.73 atm and the inlet temperature is 300 K, giving an inlet Knudsen number, based on the channel height H and the VHS mean free path, of around 0.08. Cases with inlet-to-outlet pressure ratios (p_{in}/p_{out}) of 2.5 (Case 1) and 4 (Case 2) are investigated here, using the inlet and outlet boundary algorithms described above. All surfaces are considered to be fully diffuse, with temperatures of 323 K and 523 K for T_1 and T_2, respectively. The non-uniform, non-isothermal geometry greatly increases the complexity of the channel flow problem.

The channel height H is 0.9 μm and the aspect ratio is 6.7. The steps inside the channel have a height h of 0.3 μm, a length of 1.0287 μm, and respective

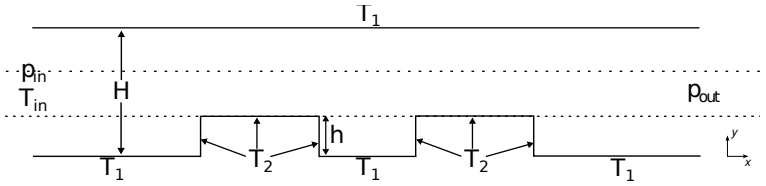

Figure 19: 2D schematic of the patterned microchannel with different wall temperatures. Dashed lines are measurement locations.

leading edge positions of 1.4787 μm and 3.4713 μm. The working gas is nitrogen, with standard VHS parameters of $\omega = 0.77$ and $d_{ref} = 4.17 \times 10^{-10}$ m at a reference temperature of 273 K, and Larsen-Borgnakke energy exchange performed on a 'single molecule' basis, where each collision partner is considered in turn for relaxation with a constant rotational relaxation number of 5. Vibrational energy is excluded from the calculations because of the relatively low temperatures involved. Many of these parameters are not defined in Fang and Liou [69], so there may be some uncertainty in the results. 7656 rectangular computational cells, and a constant time step of 1×10^{-11} s were used in the *dsmcFoam* simulations; post-processing of the results confirmed that these parameters met good DSMC practice throughout the entire domain. The *dsmcFoam* results that follow have been sampled for 200,000 time steps after steady state was achieved. Case 1 comprised around 220,000 DSMC particles, and Case 2 had 300,000. The simulations were performed in parallel on two cores of a desktop PC equipped with an i7 processor, and took around 24 hours for each simulation. Figure 20 shows the contours of overall temperature T_{ov} for Case 2.

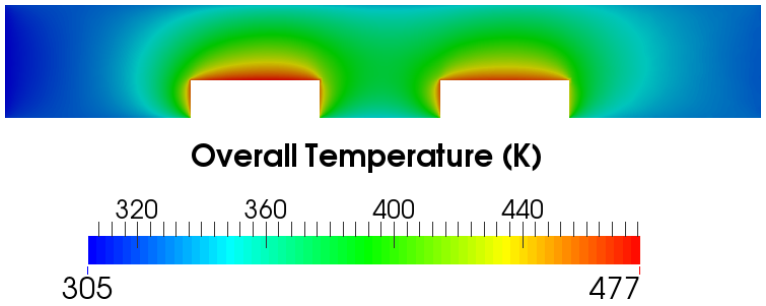

Figure 20: Contours of constant overall temperature, for $p_{in}/p_{out} = 4$.

Figure 21 shows a comparison of the overall temperature profiles for the $p_{in}/p_{out} = 2.5$ case, along two lines for the length of the channel. These two locations are illustrated by the dashed lines in Fig. 19; the first location is at the top of the steps, while the second one is mid-way between the top of the steps and the upper surface. Excellent agreement between the independent DSMC results can be seen here, with the peaks in the temperature profiles corresponding to the locations of the steps. The results for Case 2 also show excellent agreement, but have been omitted for conciseness.

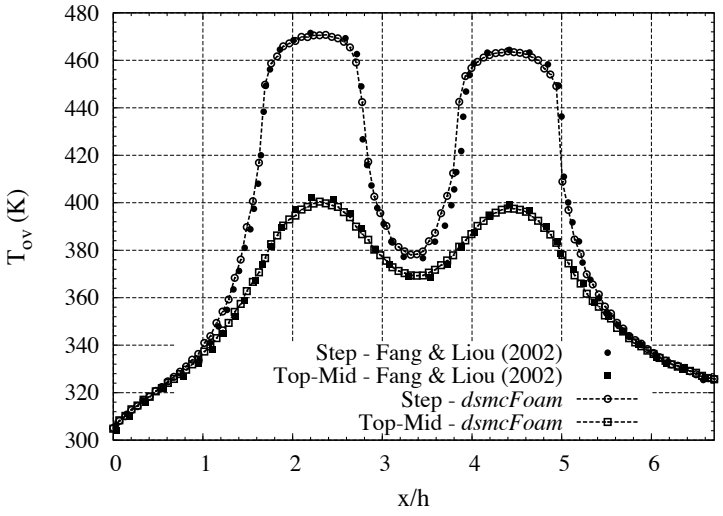

Figure 21: Comparison of temperature distribution results from from Fang and Liou [69], and *dsmcFoam* for $p_{in}/p_{out} = 2.5$.

Figure 22 shows the heat transfer at the upper surface for both $p_{in}/p_{out} = 2.5$ and 4. In general, the agreement between the DSMC results is very good, but *dsmcFoam* predicts a slightly higher heat transfer from $x/h = 2.4$ to 3.4 for both pressure ratios. The peak heat transfer around the step locations are lower for the $p_{in}/p_{out} = 4$ case, particularly at the second step, because the gas is more rarefied and so heat transfer from the gas to the surface is reduced.

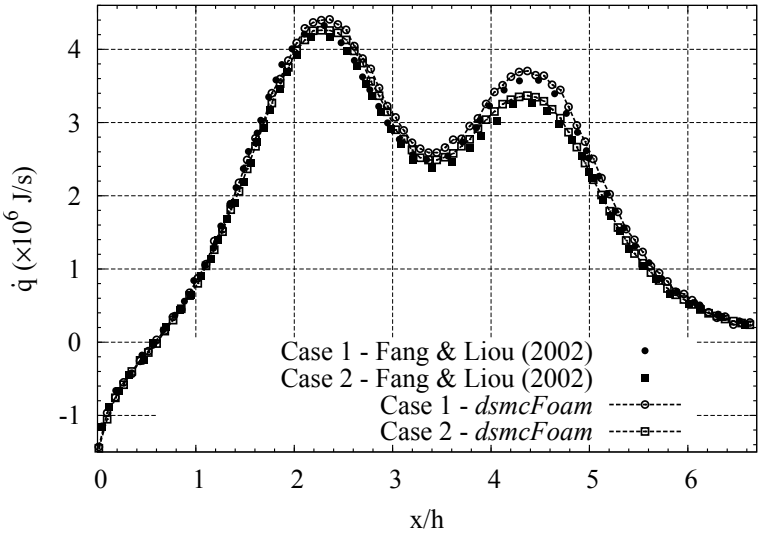

Figure 22: Comparison of the results for heat transfer at the upper surface from Fang and Liou [69] and *dsmcFoam*.

4.4. Benchmark Case D: Knudsen minimum

In order to compare micro-scale results from *dsmcFoam* to available experimental data, a series of 2D isothermal pressure-driven Poiseuille flows of nitrogen gas are solved over a large range of Knudsen number. Figure 23 is a sketch of the simple geometry.

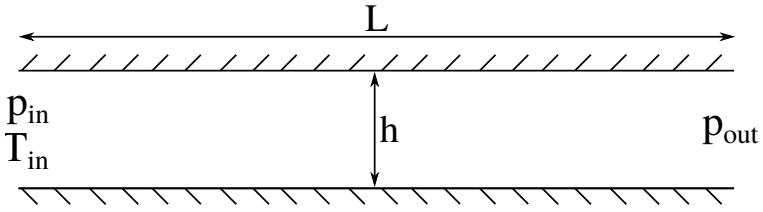

Figure 23: 2D micro-channel geometry for pressure-driven Poiseuille flow.

The variable hard sphere collision model is used with the standard nitrogen properties at a reference temperature of 273 K, i.e. viscosity coefficient $\omega = 0.74$ and reference diameter $d_{ref} = 4.17 \times 10^{-10}$ m. The mass flux $\dot{m}$ is measured

and normalized as follows:

$$Q = \frac{\dot{m} L \sqrt{2RT}}{h\,(p_{in} - p_{out})}, \tag{11}$$

where L and h are the length and height of the 2D planar Poiseuille flow channel, respectively, and R is the specific gas constant; T is the isothermal temperature that the simulations were performed at, which is 273 K. This value is used for the boundary condition of the inlet gas temperature, and is also the temperature assigned to the fully diffuse surfaces of the channel walls. The inlet pressure p_{in} and outlet pressure p_{out} are set using the boundary conditions procedure of §4.3. A rarefaction parameter δ_m is defined as the average Kn_m of the inlet and outlet Knudsen numbers (based on the VHS mean free path and the channel height h) in each case:

$$\delta_m = \frac{\sqrt{\pi}}{2Kn_m}. \tag{12}$$

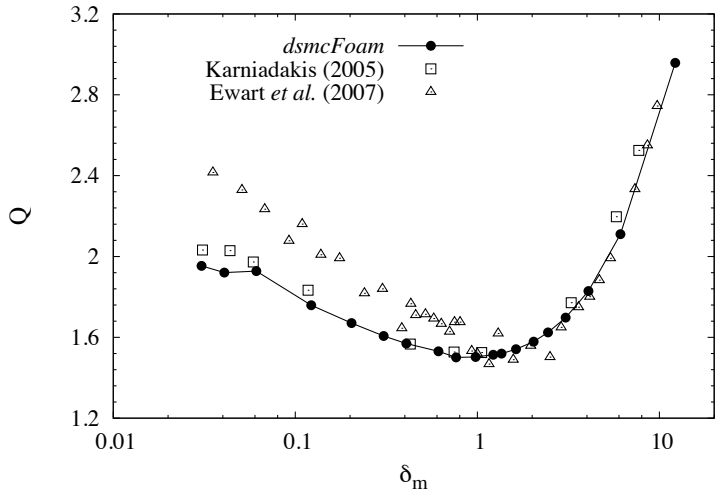

Figure 24: Normalised mass flow rate, showing the Knudsen minimum phenomenon.

The inlet to outlet pressure ratio in all cases is 3, and the aspect ratio of the planar Poiseuille geometries is 20. The gas densities are varied to achieve the different Knudsen numbers. Our *dsmcFoam* results are compared in Fig. 24 to

previous DSMC results [70] using nitrogen gas in a channel of the same aspect ratio. Experimental results from Ewart *et al.* [71], which were obtained with helium gas, are also plotted for comparison. The two sets of DSMC results are in good agreement, and the agreement with experimental data is excellent at low Kn and reasonable at high Kn. It has previously been noted [72] that the asymptotic value that Q obtains is proportional to $\ln(L/h)$; since the experimental work was performed on geometries with very large aspect ratio ($L/h = 1000$), it is expected that the DSMC results for an aspect ratio of 20 will not match exactly. Unfortunately, it is not possible to simulate an aspect ratio of 1000 using DSMC, as the velocities would be too low to obtain a converged solution in a practical time scale. The famous Knudsen minimum [73] can clearly be observed in Fig. 24, where the normalized mass flow rate has a minimum at about $Kn = 1$.

5. Conclusions

The verification and validation of new developments and features in the *dsmcFoam* code have been presented for high and speed non-reacting flows in different geometries. First, sensitivity analyses were carried out for mesh, time step, number of samples and particles was carried out for a flow over a zero-thickness flat plate. Choosing cell sizes, time steps, number of particles, and number of samples withing the ranges dictated by good DSMC practice, led to solutions that were independent of these simulation parameters.

The validation procedure aimed to compare computed *dsmcFoam* results with other numerical and experimental data available in the literature. Four different geometries were employed in the investigation: sharp and truncated flat plates, the Mars Pathfinder probe, a micro-channel with heated steps, and a simple micro-channel. In the flat plate cases, the density contours and temperature profiles showed a good concurrence between numerical and experimental data. The leading edge shape was shown clearly to influence the surface quantities. In these results, good agreement was found at the leading and trailing

edges of the sharp and truncated flat plates, respectively. In addition, conventional CFD results showed marked differences from both the DSMC simulations and experimental data, demonstrating that rarefied gas effects are not captured well by a continuum-based solver.

Hypersonic rarefied non-reacting gas flows over the Mars Pathfinder probe were also investigated. The *dsmcFoam* solver demonstrated its capabilities to successfully resolve hypersonic flows over such complex geometries. Aerodynamic surface quantities, the flow structure in the shock and wake regions, the drag, lift, and axial and normal forces acting on the probe all show a high level of agreement with CNRS experiments as well as numerical results from the DAC and MGDS codes.

In addition to the high speed benchmark cases, low speed gas flow through a micro-channel with two heated steps was considered in order to further validate the new pressure-driven *dsmcFoam* boundary conditions. The results were compared with published DSMC simulations, and an excellent level of agreement was found. In order also to compare with available micro-scale experimental data, normalized mass fluxes were calculated over a range of Knudsen numbers to demonstrate that the Knudsen minimum in Poiseuille channel flow can be captured. The results of these cases further validates the work reported in Refs. [15, 67] on subsonic, prescribed pressure inlets and outlets.

6. Acknowledgements

The authors acknowledge the financial support provided by Conselho Nacional de Desenvolvimento Científico e Tecnológico (CNPq/Brazil) under Grant No. 200473/2010-7. Our calculations were performed on the 1100 core High Performance Computing facility of the Faculty of Engineering at the University of Strathclyde.

References

[1] P. J. Roache, Need for control of numerical accuracy, Journal of Spacecraft and Rockets 27 (2) (1990) 98–102.

[2] G. Sheng, M. S. Elzas, T. I. Oren, Cronhjort, Model validation: a systemic and systematic approach, Reliability Engineering ans System Safety 42 (1993) 247–259.

[3] P. J. Roache, Verification of codes and calculations, AIAA Journal 36 (5) (1998) 696–702.

[4] P. J. Roache, Verification and validation in computational science and engineering, Hermosa Publishers, Albuquerque, NM, 1998.

[5] American Institute of Aeronautics & Astronautics Staff, AIAA guide for the verification and validation of computational fluid dynamics simulations., American Institute of Aeronautics and Astronautics, 1998.

[6] W. L. Oberkampf, T. G. Trucano, Verification and validation in computational fluid dynamics, Progress in Aerospace Sciences 38 (SAND2002-0529) (2002) 209–272.

[7] W. L. Oberkampf, T. G. Trucano, C. H. Hirsch, Verification, validation, and predictive capabilities in computational engineering and physics, Tech. Rep. 2003-3769, Sandia National Laboratories (2003).

[8] W. L. Oberkampf, M. F. Barone, Measures of agreement between computation and experiment: validation metrics, Journal of Computational Physics 217 (2006) 5–36.

[9] G. Bird, Molecular Gas Dynamics and the Direct Simulation of Gas Flows, Clarendon, Oxford, 1994.

[10] I. D. Boyd, G. Chen, G. V. Candler, Predicting failure of the continuum fluid equations in transitional hypersonic flows, Physics of Fluids 7 (1) (1995) 210–219.

[11] W. Wang, I. D. Boyd, Predicting continuum breakdown in hypersonic viscous ows, Physics of Fluids 15 (1) (2003) 91–100.

[12] J. Meng, N. Dongari, J. M. Reese, Y. Zhang, Breakdown parameter for kinetic modeling of multiscale gas flows, Physical Review E 89 (6) (2014) 063305.

[13] T. J. Scanlon, E. Roohi, C. White, M. Darbandi, J. M. Reese, An open source, parallel, DSMC code for rarefied gas flows in arbitrary geometries, Computers and Fluids 39 (2010) 2078–2089.

[14] OpenFOAM, http://www.openfoam.org/ (2014).

[15] C. White, Benchmarking, development and applications of an open source DSMC solver, Ph.D. thesis, University of Strathclyde, Glasgow, Scotland (2013).

[16] R. C. Palharini, Atmospheric reentry modelling using an open source DSMC code, Ph.D. thesis, University of Strathclyde, Glasgow, Scotland (2014).

[17] T. J. Scanlon, C. White, M. K. Borg, R. C. Palharini, E. Farbar, I. D. Boyd, J. M. Reese, R. E. Brown, Open-source direct simulation Monte Carlo chemistry modeling for hypersonic flows, AIAA Journal 53 (6) (2015) 1670–1680.

[18] M. Wang, Z. Li, Simulations for gas flows in microgeometries using the direct simulation Monte Carlo method, International Journal of Heat and Fluid Flow 25 (2004) 975–985.

[19] J. C. Lengrand, J. Allègre, A. Chpoun, M. Raffin, Rarefied hypersonic flow over a sharp flat plate: numerical and experimental results, in: 18th International Symposium on Rarefied Gas Dynamics, Vol. 160, Washington, DC, 1992, pp. 276–284.

[20] K. A. Koura, A sensitive test for accuracy in evaluation of molecular collision number in the direct-simulation Monte Carlo, Physics of Fluids A2 (7) (1990) 706–710.

[21] H. Kaburaki, M. Yokokawa, Computer simulation of two-dimensional continuum flows by the direct simulation Monte Carlo method, Molecular Simulation 12 (3-6) (1994) 441–444.

[22] C. Shu, X. H. Mao, Y. T. Chew, Particle number per cell and scaling factor effect on accuracy of dsmc simulation of micro flows, International Journal of Numerical Methods for Heat and Fluid Flow 15 (8) (2005) 827–841.

[23] Z. Sun, Z. Tang, Y. He, W. Tao, Proper cell dimension and number of particles per cell for DSMC, Computers and Fluids 50 (2011) 1–9.

[24] S. Stefanov, C. Cercignani, Monte Carlo simulation of the Taylor-Couette flow of a rarefied gas, Journal of Fluid Mechanics 256 (1993) 199–213.

[25] E. S. Piekos, K. S. Breuer, Numerical modeling of micromechanical devices using the direct simulation Monte Carlo method, Journal of Fluids Engineering 118 (3) (1996) 464–469.

[26] W. Huang, D. Bogy, Three-dimensional direct simulation Monte Carlo method for slider air bearings, Physics of Fluids 9 (6) (1997) 1764–1769.

[27] F. J. Axelander, A. G. Garcia, The direct simulation Monte Carlo method, Computer in Physics 11 (6) (1997) 588–593.

[28] D. W. Machowski, D. H. Papadopoulos, D. E. Rosner, Comparison of Burnett and DSMC predictions of pressure distribution and normal stress in one-dimensional, strong non-isothermal gases, Physics of Fluids 11 (8) (1999) 2108–2116.

[29] M. Fallavollita, D. Baganoff, J. McDonald, Reduction of simulation cost and error for particle simulation of rarefied flows, Journal of Computational Physics 109 (1) (1993) 30–36.

[30] C. Mavriplis, J. C. Ahn, R. Goulard, Heat transfer and flowfield in short microchannels using direct simulation Monte Carlo, Journal of Thermophysics and Heat Transfer 11 (4) (1997) 489–496.

[31] G. Chen, I. D. Boyd, Statistical error analysis for the direct simulation Monte Carlo technique, Journal of Computational Physics 126 (2) (1996) 434–448.

[32] S. K. Stefanov, On DSMC calculations of rarefied gas flows with small number of particle in cells, SIAM Journal of Scientific Computing 33 (2) (2011) 677–702.

[33] J. Davis, J. K. Harvey, Comparison of the direct simulated method with experiment for rarefied flat plate flow, Progress in Astronautics and Aeronautics (1963) 335–348.

[34] W. Chow, Hypersonic rarefied flow past the sharp leading edge of a flat plate, AIAA Journal 5 (9) (1967) 1549–1557.

[35] M. Becker, F. Robben, R. Cattolicai, Velocity distribution functions near the leading edge of a flat plate, AIAA Journal 12 (9) (1974) 1247–1253.

[36] W. L. Hermina, Monte Carlo simulation of rarefied flow along a flat plate, Journal of Thermophysics and Heat Transfer 3 (1989) 7–12.

[37] J. Allègre, M. Raffin, A. Chpoun, L. Gottesdiener, Rarefied hypersonic flow over a flat plate with truncated leading edge, in: 18th International Symposium on Rarefied Gas Dynamics, Vol. 160, Washington, DC, 1992, pp. 285–295.

[38] R. P. Nance, R. G. Wilmoth, B. Moon, H. A. Hassan, J. Saltz, Parallel DSMC solution of three-dimensional flow over a finite flat plate, in: 6th AIAA/ASME Joint Thermophysics and Heat Transfer Conference, Colorado Springs, CO, 1994.

[39] N. Tsuboi, H. Yamaguchi, Y. Matsumoto, Direct simulation Monte Carlo method on rarefied hypersonic flow around flat plates, Journal of Spacecraft and Rockets (3) (2004) 397–405.

[40] D. Gao, C. Zhang, T. E. Schwartzentruber, Particle simulations of planetary probe flows employing automated mesh refinement, Journal of Spacecraft and Rockets 48 (3) (2011) 397–405.

[41] C. Borgnakke, P. S. Larsen, Statistical collision model for Monte Carlo simulation of polyatomic gas mixture, Journal of Computational Physics 18 (4) (1975) 405–420.

[42] T. Tokumasu, Y. Matsumoto, Dynamic molecular collision (DMC) model for rarefied gas flow simulations by the DSMC method, Physics of Fluids 11 (7) (1999) 1907–1920.

[43] K. Koura, Null-collision technique in the direct-simulation Monte Carlo method, Physics of Fluids 29 (11) (1986) 3509–3511.

[44] G. A. Bird, Perception of numerical methods in rarefied gasdynamic, Progress in Astronautics and Aeronautics 118 (1989) 211.

[45] J. Muylaert, A. Kumar, C. Dujarric, Hypersonic experimental and computational capability, improvement and validation, North Atlantic Treaty organization, Advisory Group for Aerospace Research & Development, 1998.

[46] J. Allègre, D. Bisch, J. C. Lengrand, Experimental rarefied density flowfield at hypersonic conditions over 70–degree blunted cone, Journal of Spacecraft and Rockets 34 (6) (1997) 714–718.

[47] J. Allègre, D. Bisch, J. C. Lengrand, Experimental rarefied aerodynamic forces at hypersonic conditions over 70–degree blunted cone, Journal of Spacecraft and Rockets 34 (6) (1997) 719–723.

[48] J. Allègre, D. Bisch, J. C. Lengrand, Experimental rarefied heat transfer at hypersonic conditions over 70–degree blunted cone, Journal of Spacecraft and Rockets 34 (6) (1997) 724–728.

[49] J. N. Moss, V. K. Dogra, R. G. Wilmoth, DSMC simulations of Mach 20 nitrogen about 70-degree blunted cone and its wake, Tech. Rep. NASA TM-107762 (1993).

[50] J. N. Moss, R. A. Mitcheltree, V. K. Dogra, R. G. Wilmoth, Direct simulation Monte Carlo and navier-stokes simulations of blunt body wake flows, AIAA Journal 32 (7) (1994) 1399–1406.

[51] J. N. Moss, J. M. Price, V. K. Dogra, D. B. Hash, Comparison of DSMC and experimental results for hypersonic external flows, in: 30th Thermophysics Conference, Vol. 2028, San Diego, CA, 1995.

[52] R. P. Nance, R. G. Wilmoth, H. A. Hassan, A comparison of grid-definition schemes for DSMC, in: 34th Aerospace Sciences Meeting and Exhibit, Reno, NV, 1996.

[53] J. F. Pallegoix, Workshop ESTEC - test case no.6 - rarefied spherically blunted cone, in: 4th European High-Velocity Database Workshop, ESTEC, Noordwiwijk, The Netherlands, 1994.

[54] V. K. Dogra, J. N. Moss, J. M. Price, Near wake structure for a generic ASTV configuration, Journal of Spacecraft and Rockets 31 (6) (1996) 953–959.

[55] L. A. Gochberg, G. A. Allen, M. A. Gallis, G. S. Deiwet, Comparisons of computations and experiments for nonequilibrium flow expansions around a blunted cone, in: 34th Aerospace Sciences Meeting and Exhibit, Reno, NV, 1996.

[56] D. Hash, H. Hassan, A decoupled DSMC/Navier-Stokes analysis of a transitional flow experiment, in: 34th Aerospace Sciences Meeting and Exhibit, Vol. 353, Reno, NV, 1996, p. 1996.

[57] B. Hash, A. Hassan, Two-dimensional coupling issues of hybrid DSMC/Navier-Stokes solvers, in: 32nd Thermophysics Conference, Vol. 2507, Atlanta, GA, 1997.

[58] J. K. Harvey, M. A. Gallis, Review of code validation studies in high-speed low-density flows, Journal of Spacecraft and Rockets 37 (1) (2000) 8–20.

[59] P. A. Gnoffo, R. N. Gupta, J. L. Shinn, Conservation equations and physical models for hypersonic air flows in thermal and chemical nonequilibrium, Tech. Rep. NASA TP-2867 (1989).

[60] P. A. Gnoffo, An upwind-biased, point-implicit relaxation algorithm for viscous compressible perfect gas flows, Tech. Rep. NASA TP-2953 (1990).

[61] D. R. Olynick, H. A. Hassan, New two temperature dissociation model for reacting flows, Journal of Thermophysics and Heat Transfer 7 (4) (1993) 687–696.

[62] D. R. Olynick, J. C. Taylor, H. A. Hassan, Comparisons between Monte Carlo methods and Navier-Stokes equations for re-entry flows, Journal of Thermophysics and Heat Transfer 8 (2) (1994) 251–258.

[63] G. A. Bird, Monte-Carlo simulation in an engineering context, in: 12th International Symposium on Rarefied Gas Dynamics, Charlottesville, VA, 1981, pp. 239–255.

[64] G. J. LeBeau, A parallel implementation of the direct simulation Monte Carlo method, Computer Methods in Applied Mechanics and Engineering 174 (1999) 319–337.

[65] J. N. Moss, J. M. Price, Survey of blunt body flows including wakes at hypersonic low-density conditions, Journal of Thermophysics and Heat Transfer 11 (3) (1997) 321–329.

[66] M. J. Wright, F. S. Milos, Afterbody aeroheating flight data for planetary probe thermal protection system design, Journal of Spacecraft and Rockets 43 (5) (2006) 929–943.

[67] C. White, M. K. Borg, T. J. Scanlon, J. M. Reese, A DSMC investigation of gas flows in micro-channels with bends, Computers & Fluids 71 (2013) 261–271.

[68] R. P. Nance, D. B. Hash, H. A. Hassan, Role of boundary conditions in Monte Carlo simulation of MEMS devices, Journal of Thermophysics and Heat Transfer 12 (3) (1997) 119–128.

[69] Y. Fang, W. Liou, Computations of the flow and heat transfer in microdevices using DSMC with implicit boundary conditions, Journal of Heat Transfer 124 (2002) 338–345.

[70] G. Karniadakis, A. Beskok, N. Aluru, Microflows and Nanoflows: Fundamentals and Simulation, Springer Science+Business Media, Inc., 233 Spring St, New York, 2005.

[71] T. Ewart, P. Perrier, I. A. Graur, J. G. Méolans, Mass flow rate measurements in a microchannel, from hydrodynamic to near free molecular regimes, Journal of Fluid Mechanics 584 (2007) 337–356.

[72] N. Dongari, F. Durst, S. Chakraborty, Predicting microscale gas flows and rarefaction effects through extended Navier-Stokes-Fourier equations from phoretic transport considerations, Microfluidics and Nanofluidics 9 (2010) 831–846.

[73] W. Steckelmacher, Knudsen flow 75 years on: the current state of the art for flow of rarefied gases in tubes and systems, Reports on Progress in Physics 49 (10) (1999) 1083–1107.